Article

Ductile Fracture Prediction of X80 Pipeline Steel Using Void Growth Model

Chunjian Feng [1], Zengli Peng [2,3,*], Xin Li [2,3], Shiliu Bao [4] and Ximin Jiang [1]

[1] Offshore Department, Sinopec Petroleum Engineering Corporation, Dongying 257026, China; fengchunjian2022@163.com (C.F.); sjyjxm2006@163.com (X.J.)
[2] Research Institute of Dalian University of Technology in Shenzhen, Shenzhen 518057, China; lixin@dlut.edu.cn
[3] Faculty of Infrastructure Engineering, School of Hydraulic Engineering, Dalian University of Technology, Dalian 116024, China
[4] College of Civil and Transportation Engineering, Hohai University, Nanjing 210098, China; shiliubao@hhu.edu.cn
[*] Correspondence: pengzenli@mail.dlut.edu.cn

Abstract: In this study, the Void Growth Model (VGM) is employed to predict the ductile fracture of X80 pipeline steel. The X80 pipeline tends to be applied in challenging scenarios, such as extremely deep water and long-distance pipelines, which might cause a ductile fracture; however, the study of ductile fractures for pipeline steel is rare, especially for X80 pipeline steel. To understand ductile fractures of X80 pipeline steel, a hybrid numerical–experimental calibration method is used to determine the fracture parameter for the VGM model. The toughness capacity defined by the critical void growth index (VGI) in this study is determined to be 4.304. A shear-tension specimen is applied to verify the calibrated VGM. The results show that the calibrated VGM can predict the fracture initiation of the shear-tension specimen. In addition, the fracture of the shear-tension specimen initiates at the center of the section and propagates to the edge of the groove of the specimen. The initiation of fracture is identical to the testing observation.

Keywords: X80 pipeline steel; ductile fracture; Void Growth Model; micromechanical fracture model; finite element analysis

1. Introduction

New energy is developing rapidly, such as wind energy [1–3] and photovoltaic power [4]; however, fossil fuels are still the main source of power. High-strength steel pipelines are the major means of transportation for oil and gas in challenging conditions, such as extremely deep water [5] and long-distance pipelines [6]. The pipeline may undergo ductile fracture due to large deformations in these challenging scenarios. The ductile fracture can be defined as a process involving a significant dissipation of mechanical energy, and it undergoes a large-scale plastic deformation before the fracture [7], which is different from traditional fracture modes [8,9]. In recent years, the applicability of fracture models for pipelines and pipeline steel is focused on the traditional fracture mechanics [9–16], not the ductile fracture; however, the ductile fracture of the pipeline is inevitable [17,18], and the mechanism of the ductile fracture is complicated [7,19–24].

Various ductile fracture models were developed to predict the initiation of ductile fractures. The Gurson–Tvergaard–Needleman (GTN) model is widely used for damage accumulation and fracture prediction [25–27]. In addition, much attention has been paid to the Continuum Damage Mechanics (CDM) model [28]. The CDM model can be used in a wide range of stress states by incorporating the dependence of the stress state [29]. It is worth noting that both the GTN model and the CDM model face a challenge in calibrating the model parameters [30]. Johnson and Cook [31] assumed that the fracture strain is a

monotonic exponential function of stress triaxiality, and they developed the Johnson–Cook (J-C) model. Kanvinde et al. [32] proposed a Void Growth Model (VGM), which is widely used in the range of high-stress triaxiality. A ductile fracture is not only dependent on stress triaxiality or hydrostatic stress, but also the Lode angle. Much attention is paid to the effect of the Lode angle parameter on ductile fractures. Wierzbicki and Xue [33] proposed an empirical ductile fracture model based on the stress triaxiality and the Lode angle parameter. In some recent ductile fracture models [34–41], void growth is a function of stress triaxiality, and void coalescence is controlled by the shear stress which is related to the Lode angle parameter. These criteria improve the accuracy of prediction of the fracture strains in the middle, low, and negative stress triaxiality range. Moreover, Bai and Wierzbicki [42] proposed the Extended Mohr–Coulomb (EMC) model. The EMC model receives widespread attention, and it inspired the traditional strength theories that can be extended to the ductile fracture field. Hence, similar schemes when developing the ductile fracture criteria have been conducted, such as the Extended Hosford–Coulomb (EHC) [43] and the Extended Unified Strength Theory (EUST) [44]. According to the effects of hydrostatic stress and the Lode angle, Peng and his co-workers [7] proposed a more accurate ductile fracture model. It is worth noting that in the model proposed by Peng et al. [7] hydrostatic stress has the opposite effect on the void growth.

Several ductile fracture models were used to simulate fracture initiation. Dotta and Ruggieri [45] applied the GTN to model the ductile crack extension of longitudinal crack-like defects in X60 pipeline steel. Oh et al. [46] employed the GTN model to study the ductile fracture of X65 pipeline steel. The results of both studies showed that the GTN model can predict the ductile fracture of X60 pipeline steel and X65 pipeline steel. Kofiani et al. [47] and Paredes et al. [48] used the EMC model to study the ductility of the X70 pipeline steel, and the results indicated that the EMC model can describe fracture behavior of single edge notch tension (SENT) experiments. Testa et al. [49] applied the CDM model to predict ductile failure in X65 steel. Recently, the GTN model, the EMC model, and the extended Rice–Tracey (ERT) model were used to evaluate the ductile fracture of X80 pipeline steel [5]. In addition, the features of pipeline steel degradation after long-term operation were investigated by cutting and examining samples of local sections of pipes [24].

However, considering that most of the models are computationally expensive and difficult to calibrate, the VGM model, which needs only one parameter to define the toughness capacity, is still widely used in engineering practice. In addition, API X80 pipeline steel draws much attention because of its good performance in strength, weldability, and pressure resistance. In this study, the ductility of the X80 pipeline steel using the VGM model is investigated. The typical smooth notch tensile (SNT) tests for X80 pipeline steel were performed. To determine the parameter in the VGM model, a hybrid numerical-experimental calibration method with the SNT tests was used. Then, a shear-tension test was performed to validate the calibrated VGM model.

The paper is organized as follows. In Section 2, the theories of the VGM and the plasticity are briefly recalled. Section 3 involves two parts: we first calibrated the material constitutive parameters, then we introduced the tensile tests of X80 pipeline steel, and conducted the calibration of VGM for X80 pipeline steel based on the finite element (FE) simulation. The verification of the calibrated VGM and study of fracture behaviors of X80 pipeline steel are carried out in Section 4. In Section 5, the main conclusions are presented.

2. Theories of VGM and Plasticity

2.1. Void Growth Model

The void growth model (VGM) [32] was developed for evaluating ductile fracture under monotonic loading. The VGM is based on the analytical derivation of the growth rate of a void. For a single spherical void in an infinite continuum, the exponential void growth rate equation is derived by Rice and Tracey [50]:

$$\frac{dR}{R} = c * exp(1.5T)dp \tag{1}$$

where R is the instantaneous void radius; c is a material constant; $T = \overline{\sigma}/\sigma_{eq}$ is stress triaxiality (where $\overline{\sigma}$ is the mean stress, and σ_{eq} is the von Mises stress); dp is the incremental of equivalent plastic strain, defined to be $dp = \sqrt{(2/3)d\varepsilon_p : d\varepsilon_p}$; and $d\varepsilon_p$ is incremental with regard to the plastic strain tensor.

Integrating Equation (1), the void growth ratio under monotonic loading can be obtained:

$$ln\left(\frac{R}{R_0}\right) = \int_0^p c * exp(1.5T)dp \tag{2}$$

where R_0 is the initial void radius. From Equation (2), it can be noted that the void expansion is described in terms of a ratio of the current radius to the initial void radius. For convenience, the void growth index (VGI) η $(\eta = \ln(R/R_0)/c)$ is used, and Equation (2) is simplified as

$$\eta = \int_0^p exp(1.5T)dp \tag{3}$$

The main assumption of the model is that ductile fracture will occur when the VGI reaches a critical value, and Equation (3) yields in the following way:

$$\eta_{critical} = \int_0^{\varepsilon_f} exp(1.5T)dp \tag{4}$$

where ε_f is the ductile fracture strain. Hence, a ductile fracture criterion can be expressed as follows:

$$\eta = \int_0^p exp(1.5T)dp > \eta_{critical} \tag{5}$$

2.2. Theory of Plasticity

Under monotonic loading, several alternative modeling approaches have been proposed to simulate plastic deformation, such as the Tresca criterion [51], the Twin-shear criterion [51], the Bai–Wierzbicki criterion [52], and the Mises criterion [51]. The two former criteria have non-derivable points in the yielding plane which increase the difficulty of implementation in simulation. The Bai–Wierzbicki criterion cannot be calibrated economically; however, the Mises criterion, which is also called as the J_2 flow theory, has a smooth yield surface with only one parameter and can be used easily. More importantly, the Mises criterion is suitable for the simulation of the steel yielding, and has the following yield criterion:

$$f(\boldsymbol{\sigma}, \sigma_y) = \sqrt{3J_2(\boldsymbol{\sigma})} - \sigma_y = 0 \tag{6}$$

where $J_2(\boldsymbol{\sigma})$ is the second invariant of the stress deviator tensor; $\boldsymbol{\sigma}$ is the stress tensor; and σ_y is the size of the yield surface which represents the strain hardening behavior of a material. Several strain hardening rules were proposed to characterize the strain hardening behavior [53–55], which can be calibrated from the standard uniaxial tensile test. In theory, any hardening rule can be used if the rule describes the hardening behavior well. In this study, the Swift model [53] is suitable for the X80 pipeline steel. Hence, the Swift model [53] is used, and has the following form:

$$\sigma_y = K(\varepsilon_0 + \varepsilon_p)^n \tag{7}$$

where K and n are the strain hardening coefficient and the strain hardening exponent, respectively; ε_0 is the initial yield strain; and ε_p is the plastic part of the true strain.

3. Calibration of VGM for X80 Pipeline Steel

The VGM is typically calibrated by small-scale specimens with a notch shape. In particular, a small notch radius provides a higher stress triaxiality, whereas a large notch radius gives a lower stress triaxiality. The geometry of the typical smooth notch tensile (SNT) specimen for calibration of VGM is shown in Figure 1a. Due to the calibration for the VGM requiring the cooperation of the SNT tests and their FE simulations, the material parameters of the plastic model should be determined. Generally, the smooth round bar (SRB) specimen (see Figure 1b) is used to calibrate related material parameters.
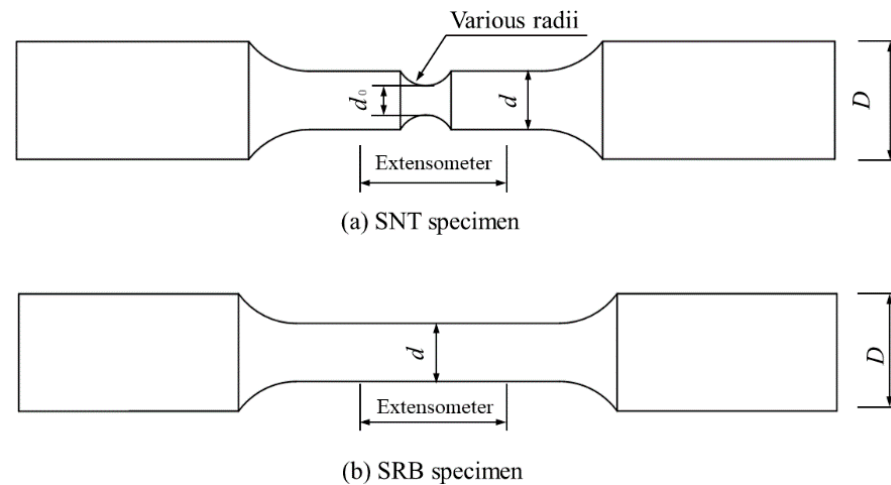

(a) SNT specimen

(b) SRB specimen

Figure 1. The geometry of specimens.

A schematic overview for the calibration program of VGM is illustrated in Figure 2. As the flowchart shows, the typical procedure includes four steps: (1) calibration of the material constitutive parameters; (2) small-scale tests; (3) FE simulation; and (4) determination of the value of toughness capacity, in other words, $\eta_{critical}$. In the first step, the parameters of the plastic model are calibrated. The monotonously axially tensile small-scale tests are loaded up for fracture in the second step. It is worth noting that the initiation of fracture is deemed to be a sudden change in slope on the load-displacement curve. In the third step, the FE simulations of the corresponding tests in the second step are conducted and the mechanical quantities related to the VGM are obtained by the postprocessing. In this study, the FE simulations are conducted in the Abaqus 6.14 (Dassault Systèmes Simulia Corp., Johnston, RI, USA) and the VGM postprocessing is based on the user-defined UVARM subroutine. The fourth step is to acquire the value of the toughness capacity $\eta_{critical}$.
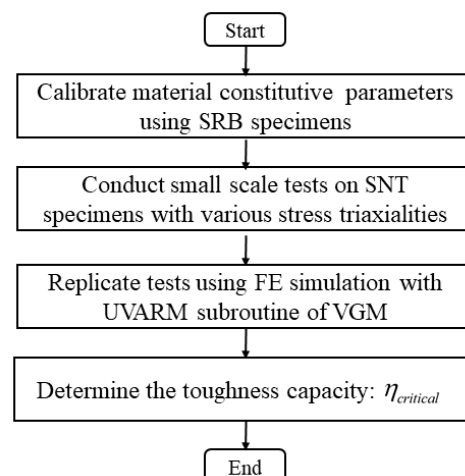

Figure 2. Flowchart of the calibration procedure for the VGM.

3.1. Calibration of the Material Constitutive Model

The smooth round bar (SRB) specimens (see Figure 3) were used to examine mechanical properties. All experimental specimens were extracted longitudinally from a pipe with 325 mm diameter and 30 mm thickness, and the tests were conducted on a Mechanical Testing & Simulation (MTS) 250 kN capacity machine (MTS, MN, USA) with a 25 mm gauge extensometer. The engineering stress and strain are determined using the following equations:

$$\sigma_{eng} = \frac{F}{A_0} \tag{8}$$

$$\varepsilon_{eng} = \frac{\Delta l}{l_0} \tag{9}$$

where F is the load force along the longitudinal direction of the SRB specimen; A_0 is the initial area of the SRB specimen; Δl indicates the elongation of the gauge; and l_0 is the initial gauge length. The results of the material property test for X80 pipeline steel are shown in Figure 4. The engineering stress–strain before necking indicates that the X80 pipeline steel has an obvious yield plateau. The mechanical properties are shown in Table 1, the average yield stress is 611 MPa, and the average Young's modulus is 203,332 MPa.
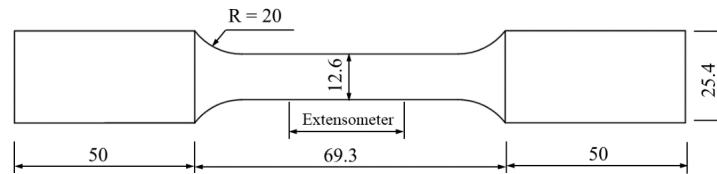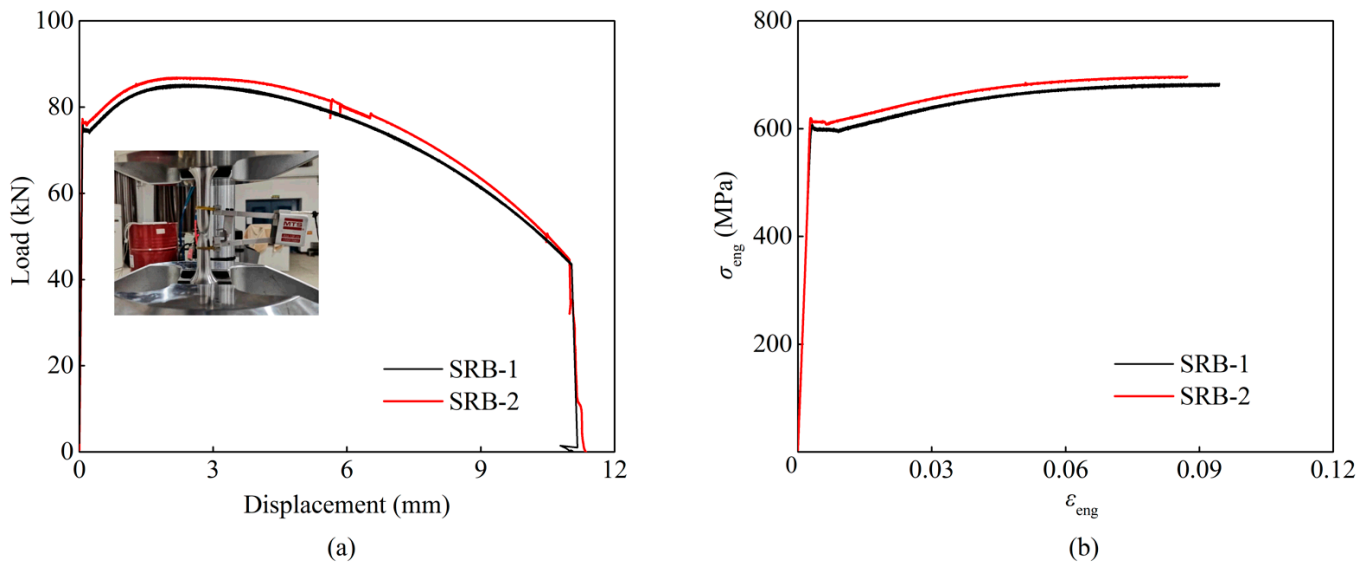

Figure 3. Geometry of SRB specimen (Unit: mm).

Figure 4. The results of the material property test for X80 pipeline steel: (**a**) the load-displacement curves; (**b**) the engineering stress-strain curve.

Table 1. Mechanical properties of X80 pipeline steel.

| Specimen No.	σ_y (MPa)	E	σ_u (MPa)	RAR (%)	K (MPa)	ε_0	n
SRB-1	600	201,769	684	75%	967	0.0127	0.116
SRB-2	622	204,894	696	74%			

Notes: σ_y is yield stress; σ_u is ultimate tensile stress; E is young's modulus; RAR is the written abbreviation of Ratio of Area Reduction.

The true stress and strain can be converted from the engineering stress and strain (see Figure 4b). The Swift hardening law was selected to extend the stress and strain relationship after necking. The resulting Swift hardening law parameters are listed in Table 1.

3.2. Calibration of VGM

The smooth notched tensile (SNT) specimens of X80 pipeline steel were tested at room temperature. The notch radii are 1.5 mm, 3.2 mm, and 6.3 mm, respectively. As mentioned above, the SNT specimens were loaded for fracture. The tests were conducted on a 250 kN capacity MTS machine with a 25 mm gauge extensometer. Figure 5 presents the test scene and the specimen geometry, and the test results are specified in Table 2.

To determine the toughness capacity $\eta_{critical}$ from the SNT test results, FE models for all tests were replicated in Abaqus 6.14 to obtain the stress and strain field in the gauge length. As illustrated in Figure 5c, the FE model was established by the axisymmetric elements. The four-node bilinear axisymmetric element, CAX4R, was used to discretize the FE model, and the element size at the center of the section is about 0.2 mm. More importantly, the mechanical quantities related to the VGM were calculated by the UVARM subroutine.
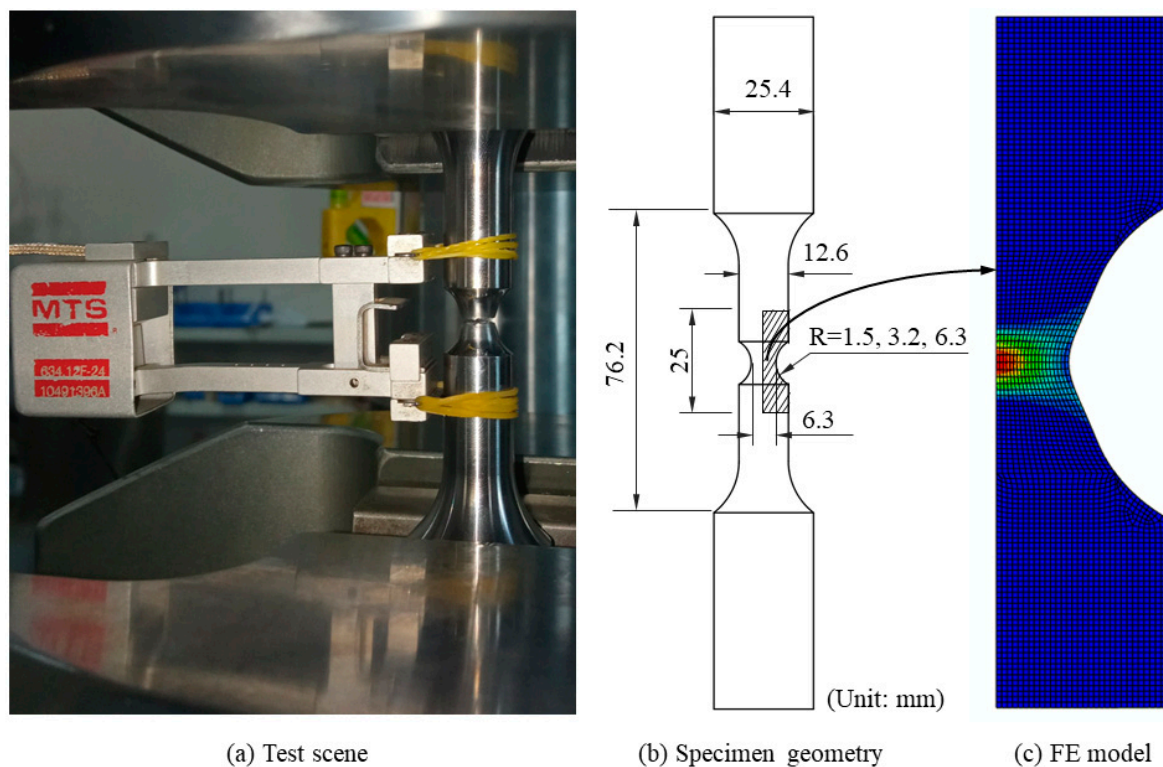
(a) Test scene (b) Specimen geometry (c) FE model

Figure 5. Illustration of X80 pipeline steel specimen.

Table 2. Test results of the X80 pipeline steel.

Load and Displacement at the Fracture	Specimens					
	R = 1.5 mm		R = 3.2 mm		R = 6.3 mm	
	M1	M2	M3	M4	M5	M6
F_f (kN)	33.7	33.1	27.9	29.6	25.7	25.6
Δ_f (mm)	0.856	0.883	1.673	1.596	2.351	2.315

Notes: The combination of the number and letter is a label of test, where M indicates a tensile test. F_f and Δ_f refer to the maximum load and the displacement at the fracture initiation, respectively.

The experimental and numerical load-displacement results are shown in Figures 6–8. The sudden change in slope of the experimental load-displacement curve, indicating the

fracture initiation, is marked as a black circle. It was observed that the finite element analysis (FEA) method, and the calibrated material parameters, provide a good agreement between the experimental and numerical load-deformation responses of the tensile tests.
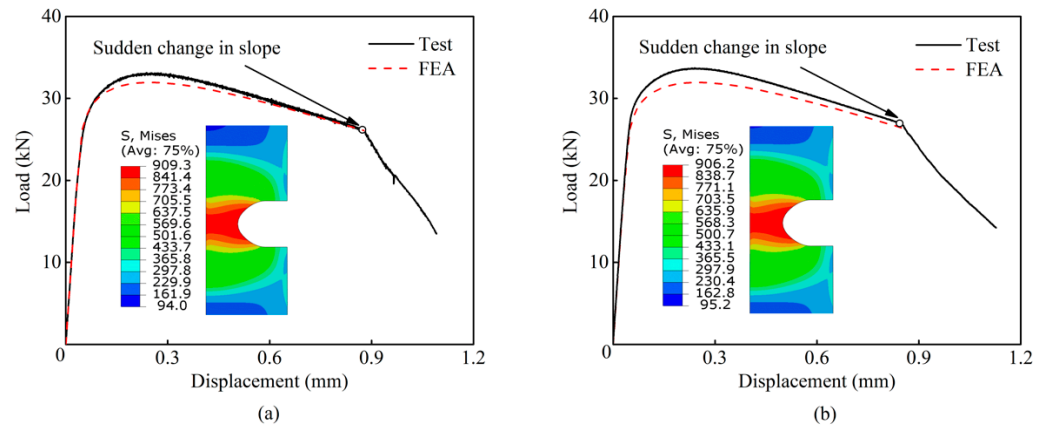

Figure 6. Numerical results of X80 pipeline steel for the SNT tensile specimens (R = 1.5 mm): (**a**) Specimen M1; (**b**) Specimen M2.
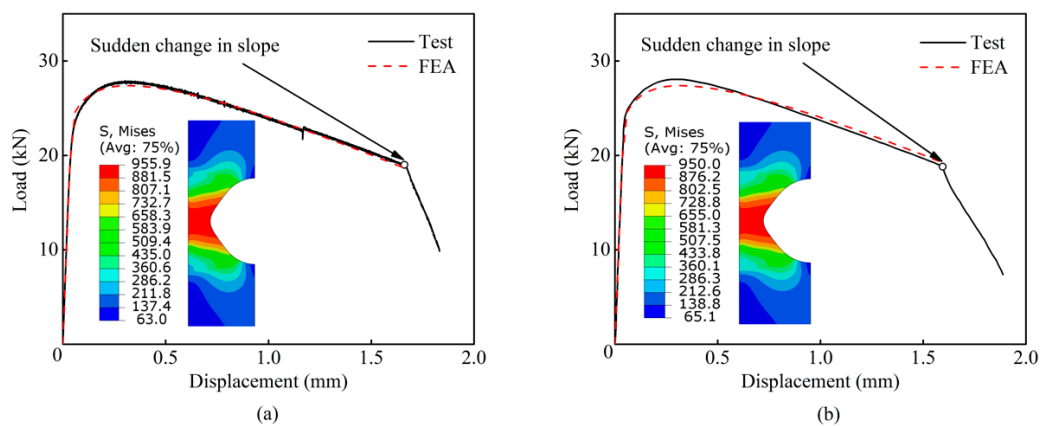

Figure 7. Numerical results of X80 pipeline steel for the SNT tensile specimens (R = 3.2 mm): (**a**) Specimen M3; (**b**) Specimen M4.
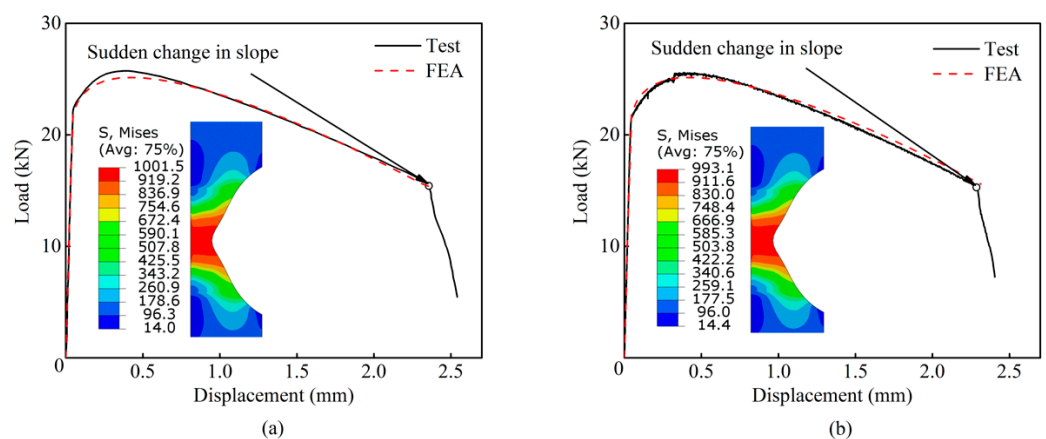

Figure 8. Numerical results of X80 pipeline steel for the SNT tensile specimens (R = 6.3 mm): (**a**) Specimen M5; (**b**) Specimen M6.

Figure 9 presents the stress state for SNT tensile specimens, including equivalent plastic strain and stress triaxiality over notch sections. It is found in Figure 9a that the

distribution of equivalent plastic strain of the three SNT specimens over the notch section is relatively uniform, and a smaller notch radius of the SNT specimen produces less equivalent plastic strain. As to the stress triaxiality (see Figure 9b), the distributions of the three SNT specimens are non-uniform over the notch section, and the highest stress triaxiality is at the center of the section. More importantly, a smaller notch radius of the SNT specimen causes higher stress triaxiality; therefore, the critical point of the SNT specimen for the fracture initiation is located at the center of the section. The contours of the VGI of the three SNT specimens (Figure 10) show that the maximum values of VGI are located at the center of the section.
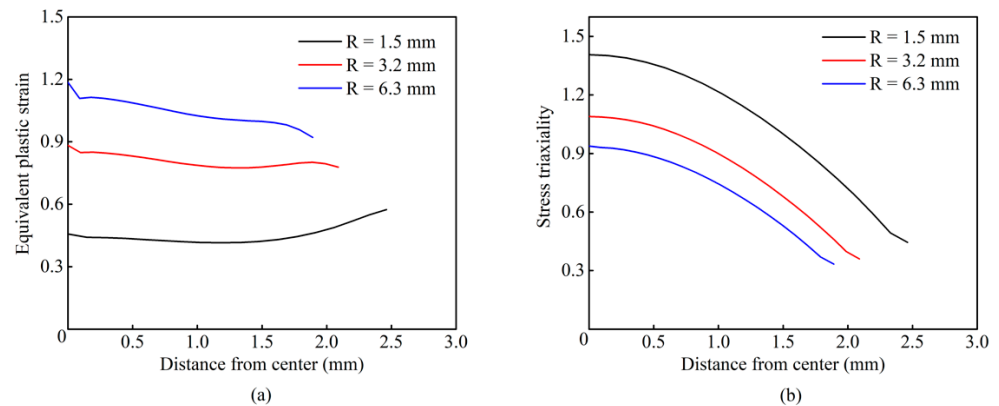

(a)   (b)

Figure 9. Distribution of stress triaxiality and equivalent plastic strain over notch section for SNT tensile specimens (M1, M3, and M5): (**a**) stress triaxiality; and (**b**) equivalent plastic strain.
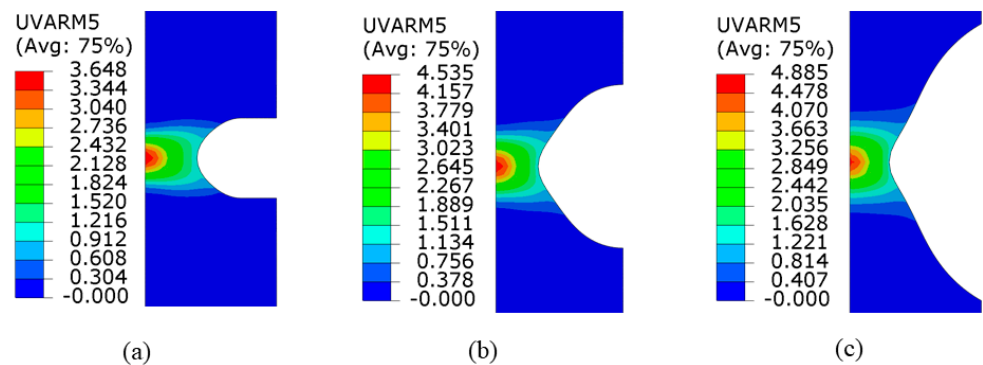

(a)   (b)   (c)

Figure 10. VGI distribution at fracture initiation: (**a**) Specimen M1 (R = 1.5 mm); (**b**) Specimen M3 (R = 3.2 mm); and (**c**) Specimen M5 (R = 6.3 mm).

The plot of equivalent plastic strain versus stress triaxiality at the center of the notch section is shown in Figure 11. It is found that the stress triaxiality is not constant as the plastic deformation develops. To estimate the level of the triaxiality for a loading procedure, the average stress triaxiality $\overline{T}$ is defined as:

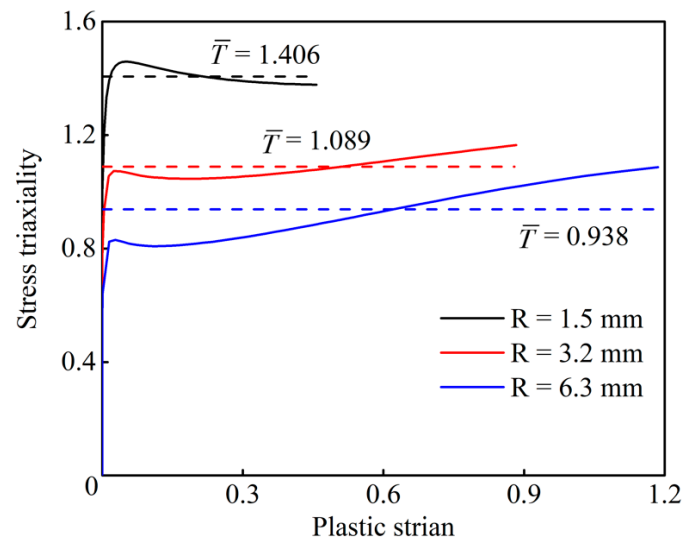$$\overline{T} = \frac{1}{\varepsilon_f} \int_0^{\varepsilon_f} T dp \tag{10}$$

Figure 11. Equivalent plastic strain versus stress triaxiality for X80 pipeline steel SNT tensile specimens (M1, M3, and M5).

The stress and strain quantities corresponding to VGM are shown in Table 3. The average stress triaxiality varies in a high-stress triaxiality interval, and the ductile fracture strains indicate that X80 pipeline steel possesses good ductility. The toughness capacity (the average value of $\eta_{critical}$) is determined to be 4.304.

Table 3. Calibration of $\eta_{critical}$ in VGM.

Specimen No.	$\overline{T}$	ε_f	$\eta_{critical}$
M1	1.406	0.442	3.648
M2	1.406	0.457	3.768
M3	1.089	0.883	4.535
M4	1.089	0.838	4.276
M5	0.938	1.186	4.885
M6	0.933	1.153	4.714
The average value			4.304

4. Verification of Calibrated VGM and Fracture Behaviors of X80 Pipeline Steel

A monotonic tensile test was conducted on a shear-tension specimen (see Figure 12) to verify the calibrated material parameters. The shear-tension specimen was fabricated from the same X80 pipeline, which was mentioned in Section 3.1. The test was conducted on a 100 kN capacity MTS machine with a 20 mm gauge extensometer. It can be observed that the fracture initiation is located in the center of the slant groove and the fracture propagates from the center to the edge of the notch. The corresponding FE simulation was performed in Abaqus to obtain the stress and strain field in the gauge length. As shown in Figure 12c, the FE model was established by 3D solid elements. The eight-node linear brick element with reduced integration, C3D8R, was used to discretize the FE model, and the element size at the center of the notch is about 0.15 mm. To improve efficiency, half of the test specimen was modeled.
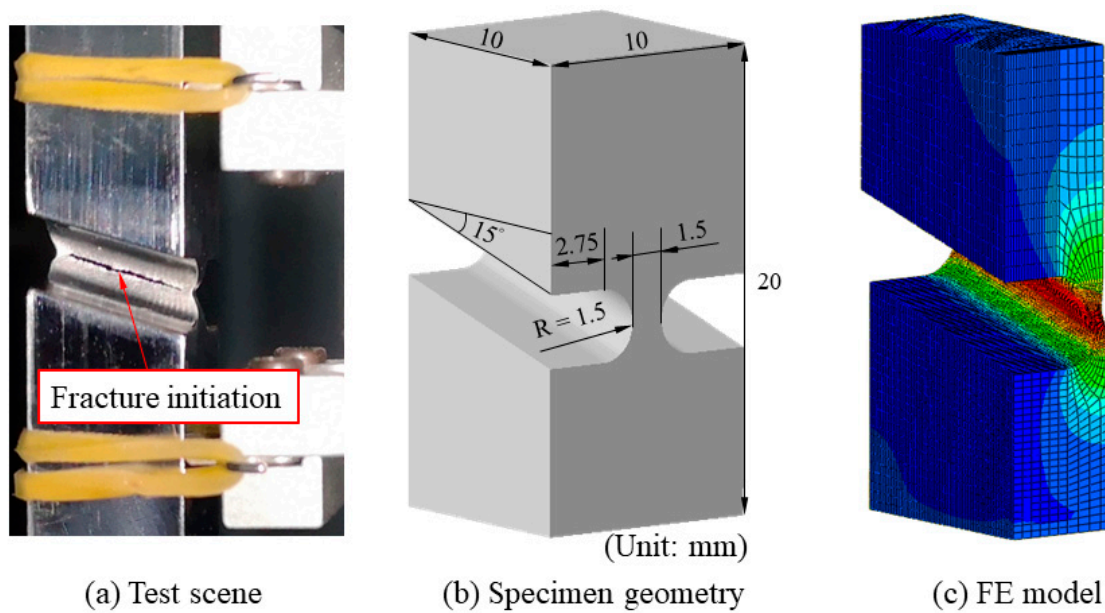
(a) Test scene   (b) Specimen geometry   (c) FE model

Figure 12. Illustration of X80 pipeline steel specimen.

The UVARM subroutine with calibrated VGM was used to predict the fracture initiation of the shear-tension specimen. The criterion for the end of simulation was that VGI needed to reach the critical value of 4.304. The comparison between the test and predicted load-displacement (see Figure 13) curves shows that the calibrated VGM can predict the fracture initiation of the tested shear-tension specimen. The error of the predicted displacement is 3%.
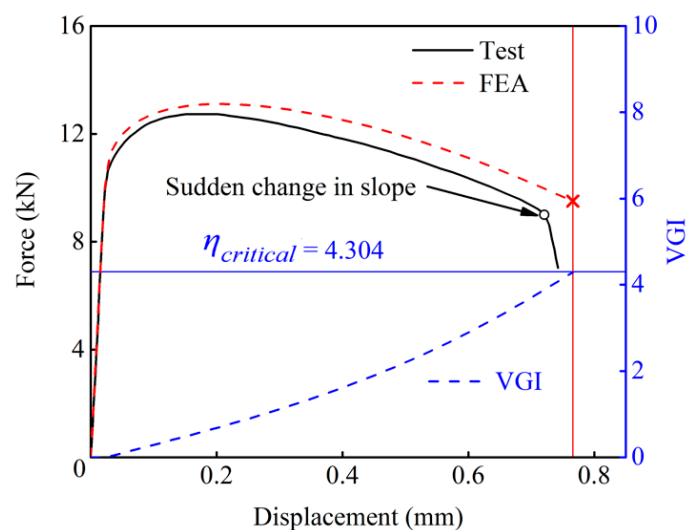

Figure 13. Lode-displacement curve and VGI evolution of the shear-tension specimen.

To understand the initiation of fracture, the distributions of the related mechanical quantities are explored. The contour of the von Mises stress (see Figure 14) shows that the Mises stress at the notch root is relatively uniform. The distribution of the VGI (see Figure 15) shows that the void growth is localized at the center of the slant groove, and the VGI decreases sharply from the center to the edge of the groove. The distributions of equivalent plastic strain and stress triaxiality along the specified paths (see Figure 16) indicates that the fracture initiation is at the center of the section; therefore, it can be concluded that the fracture of the shear-tension specimen is initiated at the center of the

slant groove and propagates to the edge of the section. The initiation of fracture is identical to the testing observation.
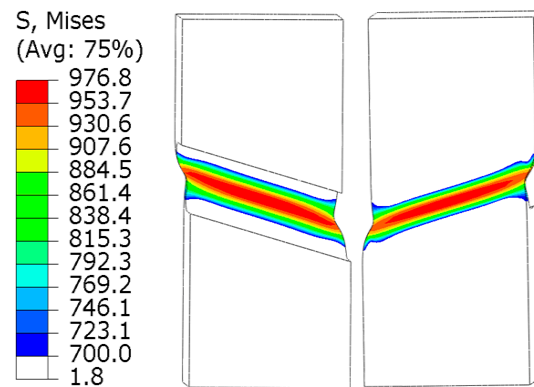

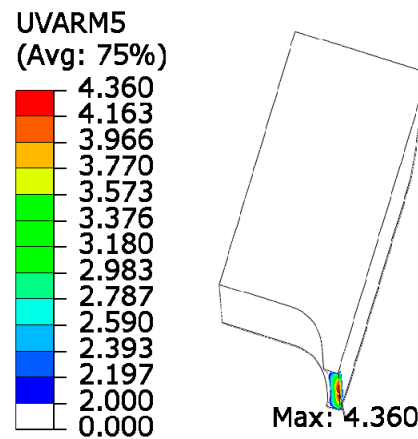**Figure 14.** The contour of the von Mises stress.
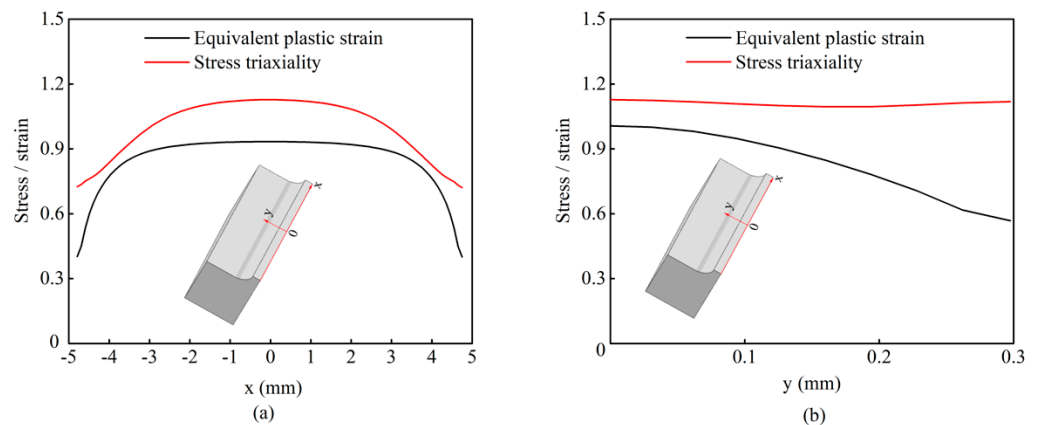

Figure 15. The contour of the VGI.

Figure 16. Distributions of equivalent plastic strain and stress triaxiality along the specified paths: (**a**) x-axis; (**b**) y-axis.

5. Application and Limitation of the VGM Model in Estimating Real Pipelines

Offshore steel pipes can be subjected to quite complex and severe loads during installation and/or operation. More importantly, the local flaw of the pipe, such as a dent [56], corrosion [57], or gouge [58], can localize the deformation with large-scale yielding, and lead to a ductile fracture featured in the large-scale yielding of the steel and the non-pre-cracked body. It is noted that the ductile fracture is beyond the scope of traditional fracture

mechanics; hence, the ductile fracture is an important consideration for the integrity assessment of offshore pipelines, and a local ductile fracture criterion is needed. The VGM model used in this study is a local ductile fracture criterion with the mechanism of void growth. In practice, the calibrated VGM can be used to estimate the integrity of pipelines in four steps (see Figure 17): (1) identify the stress state and local flaw of pipelines; (2) build a fine FE model for the pipelines; (3) verify the FE model by the full-scale experiment; and (4) estimate the integrity of pipelines using the calibrated VGM embedded in the FE model. However, the VGM model is suitable for ductile fractures in a high-stress triaxiality range which is dominated by the mechanism of void growth; hence, attention to the scope of the VGM should be paid. In the ongoing research work, full-scale experiments on the pipelines have been conducted to simulate the real loading environment. More importantly, the VGM will be embedded in the FE model to predict the ductile fracture of the full-scale experiments.
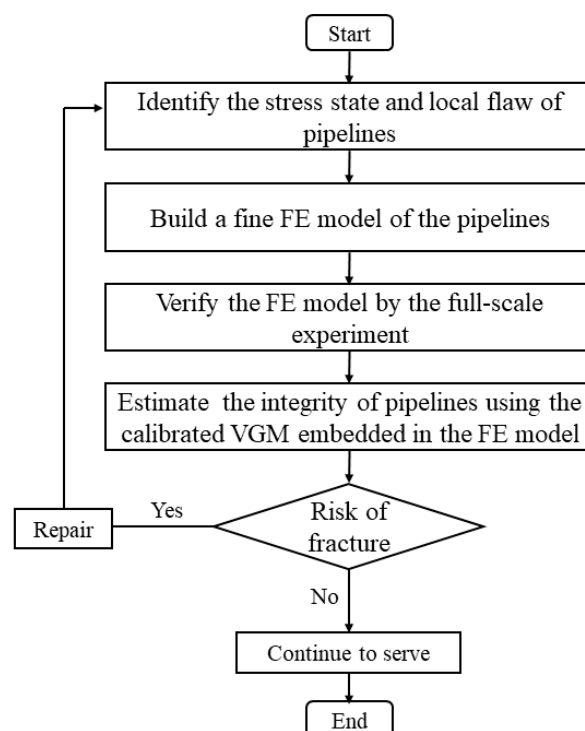

Figure 17. Flowchart of application of the calibrated VGM for the real pipelines.

6. Conclusions

In this study, the ductility of the X80 pipeline steel using the VGM model is investigated. Tests of smooth round bar specimens were conducted to calibrate the constitutive parameters of the material, and typical smooth notch tensile tests for X80 pipeline steel were performed. To determine the parameter in the VGM, finite element analysis (FEA) corresponding to the SNT tests was conducted. In addition, the shear-tension test was performed to validate the calibrated VGM. The main conclusions of the research are summarized as follows:

(1) The material parameter in the VGM was calibrated by tests and corresponding FEA. The parameter $\eta_{critical}$ in the VGM is determined as 4.304. Moreover, the Swift hardening law parameters of X80 pipeline steel are determined as: $K = 967$ MPa, $\varepsilon_0 = 0.0127$, and $\varepsilon_p = 0.116$.

(2) The calibrated material parameter in the VGM was verified by the test on a shear-tension specimen subjected to monotonic tension. The VGM gave accurate predictions of fracture initiation of the test specimen.

(3) The fracture of the shear-tension specimen initiates at the center of the groove and propagates to the edge of the section. The initiation of fracture is identical to the testing observation.

References

1. Ren, Y.; Venugopal, V.; Shi, W. Dynamic analysis of a multi-column TLP floating offshore wind turbine with tendon failure scenarios. *Ocean Eng.* **2022**, *245*, 110472. [CrossRef]
2. Zhang, L.; Shi, W.; Karimirad, M.; Michailides, C.; Jiang, Z. Second-order hydrodynamic effects on the response of three semisubmersible floating offshore wind turbines. *Ocean Eng.* **2020**, *207*, 107371. [CrossRef]
3. Wang, Y.; Shi, W.; Michailides, C.; Wan, L.; Kim, H.; Li, X. WEC shape effect on the motion response and power performance of a combined wind-wave energy converter. *Ocean Eng.* **2022**, *250*, 11103. [CrossRef]
4. Qiu, T.; Wang, L.; Lu, Y.; Zhang, M.; Qin, W.; Wang, S.; Wang, L. Potential assessment of photovoltaic power generation in China. *Renew. Sustain. Energy Rev.* **2021**, *154*, 111900. [CrossRef]
5. Han, P.; Cheng, P.; Yuan, S.; Bai, Y. Characterization of ductile fracture criterion for API X80 pipeline steel based on a phenomenological approach. *Thin-Walled Struct.* **2021**, *164*, 107254. [CrossRef]
6. Gräf, M.K.; Hillenbrand, H.G.; Heckmann, C.J.; Niederhoff, K.A. High-strength large-diameter pipe for long-distance high pressure gas pipelines. In Proceedings of the Thirteenth International Offshore and Polar Engineering Conference, Honolulu, HI, USA, 25–30 May 2003.
7. Peng, Z.; Zhao, H.; Li, X. New ductile fracture model for fracture prediction ranging from negative to high stress triaxiality. *Int. J. Plast.* **2021**, *145*, 103057. [CrossRef]
8. Anderson, T. *Fracture Mechanics: Fundamentals and Applications*, 4th ed.; Taylor & Francis Group, LLC: Boca Raton, FL, USA, 2017.
9. Zhao, H.; Lie, S. Determination of dimensionless stress intensity factor of plate-to-plate butt welds between axially aligned members of different thickness. *Eng. Fract. Mech.* **2017**, *172*, 90–105. [CrossRef]
10. Zhao, H.; Lie, S.; Vipin, S. New weld toe magnification factors for semi-elliptical cracks in plate-to-plate butt-welded joints. *Fatigue Fract. Eng. Mater. Struct.* **2017**, *40*, 207–220.
11. Zhao, H.; Lie, S.; Zhang, Y. Elastic-plastic fracture analyses for misaligned clad pipeline containing a canoe shape surface crack subjected to large plastic deformation. *Ocean Eng.* **2017**, *146*, 87–100. [CrossRef]
12. Zhao, H.; Lie, S.; Zhang, Y. Fatigue assessment of cracked pipes with weld misalignment by using stress intensity factors. *Int. J. Fatigue* **2018**, *116*, 192–209. [CrossRef]
13. Lie, S.; Zhao, H. Fracture analysis of load-carrying cruciform fillet welded joints with multiple cracks. *Eng. Fract. Mech.* **2018**, *193*, 32–46. [CrossRef]
14. Zhao, H.; Lie, S.; Zhang, Y. Fracture assessment of mismatched girth welds in oval-shaped clad pipes subjected to bending moment. *Int. J. Press. Vessel. Pip.* **2018**, *160*, 1–13. [CrossRef]
15. Zhao, H.; Li, X.; Lie, S. Strain-based fracture assessment for an interface crack in clad pipes under complicated loading conditions. *Ocean Eng.* **2020**, *198*, 106992. [CrossRef]
16. Zhao, H.; Lie, S.; Zhang, Y. Strain-based J-estimation scheme for fracture assessment of misaligned clad pipelines with an interface crack. *Mar. Struct.* **2018**, *61*, 238–255. [CrossRef]
17. Zhao, H.; Lie, S.; Zhang, Y. Stress intensity factors for semi-elliptical surface cracks in plate-to-plate butt welds with parallel misalignment of same thickness. *Mar. Struct.* **2017**, *53*, 148–163. [CrossRef]
18. Sun, M.; Zhao, H.; Li, X.; Liu, J.; Xu, Z. A new evaluation method for burst pressure of pipeline with colonies of circumferentially aligned defects. *Ocean Eng.* **2021**, *222*, 108628. [CrossRef]
19. Sun, M.; Zhao, H.; Li, X.; Liu, J.; Xu, Z. New evaluation method of failure pressure of steel pipeline with irregular-shaped defect. *Appl. Ocean Res.* **2021**, *110*, 102601. [CrossRef]
20. Brünig, M.; Gerke, S.; Koirala, S. Biaxial experiments and numerical analysis on stress-state-dependent damage and failure behavior of the anisotropic aluminum alloy EN AW-2017A. *Metals* **2021**, *11*, 1214. [CrossRef]

21. Algarni, M.; Bai, Y.; Zwawi, M.; Ghazali, S. Damage evolution due to extremely low-cycle fatigue for inconel 718 alloy. *Metals* **2019**, *9*, 1109. [CrossRef]
22. Peng, J.; Wang, Y.; Dai, Q.; Liu, X.; Zhang, Z. Effect of stress triaxiality on plastic damage evolution and failure mode for 316l notched specimen. *Metals* **2019**, *9*, 1067. [CrossRef]
23. Zhu, Y.; Huang, S.; Sajid, H. Micro-mechanisms and modeling of ductile fracture initiation in structural steel after exposure to elevated temperatures. *Metals* **2021**, *11*, 767. [CrossRef]
24. Hutsaylyuk, V.; Maruschak, P.; Konovalenko, I.; Panin, S.; Bishchak, R.; Chausov, M. Mechanical properties of gas main steels after long-term operation and peculiarities of their fracture surface morphology. *Materials* **2019**, *12*, 491. [CrossRef] [PubMed]
25. Gurson, A. Continuum theory of ductile rupture by void nucleation and growth: Part 1—Yield criteria and flow rules for porous ductile media. *J. Eng. Mater. Technol.* **1977**, *99*, 2–15. [CrossRef]
26. Tvergaard, V.; Needleman, A. Analysis of the cup-cone fracture in a round tensile bar. *Acta Met.* **1984**, *32*, 157–169. [CrossRef]
27. Tvergaard, V. Influence of voids on shear band instabilities under plane strain conditions. *Int. J. Fract.* **1981**, *17*, 389–407. [CrossRef]
28. Lemaitre, J. A Continuous damage mechanics model for ductile fracture. *J. Eng. Mater. Technol.* **1985**, *107*, 83–89. [CrossRef]
29. Brünig, M.; Gerke, S.; Schmidt, M. Damage and failure at negative stress triaxialities: Experiments, modeling and numerical simulations. *Int. J. Plast.* **2018**, *102*, 70–82. [CrossRef]
30. Khan, A.; Liu, H. A new approach for ductile fracture prediction on Al 2024-T351 alloy. *Int. J. Plast.* **2012**, *35*, 1–12. [CrossRef]
31. Johnson, G.; Cook, W. Fracture characteristics of three metals subjected to various strains, strain rates, temperatures and pressures. *Eng. Fract. Mech.* **1985**, *1*, 31–48. [CrossRef]
32. Kanvinde, A.; Deierlein, G. The void growth model and the stress modified critical strain model to predict ductile fracture in structural steels. *J. Struct. Eng.* **2006**, *132*, 1907–1918. [CrossRef]
33. Wierzbicki, T.; Bao, Y.; Lee, Y.-W.; Bai, Y. Calibration and evaluation of seven fracture models. *Int. J. Mech. Sci.* **2005**, *47*, 719–743. [CrossRef]
34. Lou, Y.; Chen, L.; Clausmeyer, T.; Tekkaya, A.E.; Yoon, J.W. Modeling of ductile fracture from shear to balanced biaxial tension for sheet metals. *Int. J. Solids Struct.* **2017**, *112*, 169–184. [CrossRef]
35. Lou, Y.; Yoon, J.; Huh, H. Modeling of shear ductile fracture considering a changeable cut-off value for stress triaxiality. *Int. J. Plast.* **2014**, *54*, 56–80. [CrossRef]
36. Lou, Y.; Huh, H.; Lim, S.; Pack, K. New ductile fracture criterion for prediction of fracture forming limit diagrams of sheet metals. *Int. J. Solids Struct.* **2012**, *49*, 3605–3615. [CrossRef]
37. Wen, H.; Mahmoud, H. New model for ductile fracture of metal alloys. I: Monotonic loading. *J. Eng. Mech.* **2016**, *2*, 4015088. [CrossRef]
38. Hu, Q.; Zhang, F.; Li, X.; Chen, J. Overview on the prediction models for sheet metal forming failure: Necking and ductile fracture. *Acta Mech. Solida Sin.* **2018**, *31*, 259–289. [CrossRef]
39. Mu, L.; Zang, Y.; Wang, Y.; Li, X.L.; Stemler, P.M.A. Phenomenological uncoupled ductile fracture model considering different void deformation modes for sheet metal forming. *Int. J. Mech. Sci.* **2018**, *141*, 408–423. [CrossRef]
40. Zhu, Y.; Engelhardt, M. Prediction of ductile fracture for metal alloys using a shear modified void growth model. *Eng. Fract. Mech.* **2018**, *190*, 491–513. [CrossRef]
41. Quach, H.; Kim, J.-J.; Nguyen, D.-T.; Kim, Y.-S. Uncoupled ductile fracture criterion considering secondary void band behaviors for failure prediction in sheet metal forming. *Int. J. Mech. Sci.* **2020**, *169*, 105297. [CrossRef]
42. Bai, Y.; Wierzbicki, T. Application of extended Mohr-Coulomb criterion to ductile fracture. *Int. J. Fract.* **2010**, *161*, 1. [CrossRef]
43. Mohr, D.; Marcadet, S. Micromechanically-motivated phenomenological Hosford-Coulomb model for predicting ductile fracture initiation at low stress triaxialities. *Int. J. Solids Struct.* **2015**, *67–68*, 40–55. [CrossRef]
44. Wang, P.; Qu, S. Analysis of ductile fracture by extended unified strength theory. *Int. J. Plast.* **2018**, *104*, 196–213. [CrossRef]
45. Dotta, F.; Ruggieri, C. Structural integrity assessments of high pressure pipelines with axial flaws using a micromechanics model. *Int. J. Press. Vessel. Pip.* **2004**, *81*, 761–770. [CrossRef]
46. Oh, C.-K.; Kim, Y.-J.; Baek, J.-H.; Kim, Y.-P.; Kim, W. A phenomenological model of ductile fracture for API X65 steel. *Int. J. Mech. Sci.* **2007**, *49*, 1399–1412. [CrossRef]
47. Kofiani, K.; Nonn, A.; Wierzbicki, T. New calibration method for high and low triaxiality and validation on SENT specimens of API X70. *Int. J. Press. Vessel. Pip.* **2013**, *111–112*, 187–201. [CrossRef]
48. Paredes, M.; Wierzbicki, T.; Zelenak, P. Prediction of crack initiation and propagation in X70 pipeline steels. *Eng. Fract. Mech.* **2016**, *168*, 92–111. [CrossRef]
49. Testa, G.; Bonora, N.; Gentile, D.; Carlucci, A.; Madi, Y. Ductile fracture assessment of X65 steel using damage mechanics. *Procedia Struct. Integr.* **2017**, *3*, 508–516. [CrossRef]
50. Rice, J.; Tracey, D. On the ductile enlargement of voids in triaxial stress fields. *J. Mech. Phys. Solids* **1969**, *3*, 201–217. [CrossRef]
51. Yu, M. Advances in strength theories for materials under complex stress state in the 20th Century. *Appl. Mech. Rev.* **2002**, *3*, 169–218. [CrossRef]
52. Bai, Y.; Wierzbicki, T. A new model of metal plasticity and fracture with pressure and Lode dependence. *Int. J. Plast.* **2008**, *24*, 1071–1096. [CrossRef]
53. Swift, H. Plastic instability under plane stress. *J. Mech. Phys. Solids* **1952**, *1*, 1–18. [CrossRef]

54. Tu, S.; Ren, X.; He, J.; Zhang, Z. Stress-strain curves of metallic materials and post-necking strain hardening characterization: A review. *Fatigue Fract. Eng. Mater. Struct.* **2019**, *43*, 3–19. [CrossRef]

55. Sung, J.; Kim, J.; Wagoner, R. A plastic constitutive equation incorporating strain, strain-rate, and temperature. *Int. J. Plast.* **2010**, *26*, 1746–1771. [CrossRef]

56. Luo, J.; Zhang, Y.; Li, L.; Zhu, L.; Wu, G. Fatigue failure analysis of dented pipeline and simulation calculation. *Eng. Fail. Anal.* **2020**, *113*, 104572. [CrossRef]

57. Gao, J.; Peng, Z.; Li, X.; Zhou, J.; Zhou, W. Bending capacity of corroded pipeline subjected to internal pressure and axial loadings. In Proceedings of the ASME 2018 37th International Conference on Ocean, Offshore and Arctic Engineering, Madrid, Spain, 17–22 June 2018; Volume 3.

58. Tee, K.; Wordu, A. Burst strength analysis of pressurized steel pipelines with corrosion and gouge defects. *Eng. Fail. Anal.* **2020**, *108*, 104347. [CrossRef]